Tracking single charge jumping with an individual color center in diamond

C. F. Weng, S. R. Lin, J. X. Zhao, Y. J. Yang, M. Y. Cai, Y. H. Guo, L. R. Lou, W. Zhu, and G. Z. Wang
Key Laboratory of Strongly-Coupled Matter Physics, Chinese Academy of Sciences, and Department of Physics, University of Science and Technology of China, Hefei, Anhui 230026, People's Republic of China

(Received 4 November 2023; revised 23 February 2024; accepted 10 May 2024; published 5 June 2024)

Acquiring knowledge about the internal field environment of a solid-state spin is essential for its effective utilization as an external field detector. Working with the nitrogen-vacancy (NV) center in our diamond sample, we observed that almost all the NV centers with high effective field near the diamond surface has two sets of ODMR which we refer to as two states. Remarkably, near room temperature, these NV centers can spontaneously transition between these two states. Our experiments demonstrate that for NV centers with high ODMR splitting and shifting, the effective field cannot be solely attributed to a pure electric field. By sweeping the polarization direction of the microwave (MW) driving field, we extract both the strength and direction of the effective field. Furthermore, we track the real-time behavior of charges within the diamond by monitoring alternations in the Rabi frequencies, providing deeper insight into their hopping dynamics. These findings suggest the potential for manipulating NV centers by regulating the surrounding charge environment.

DOI: 10.1103/PhysRevB.109.224104

Introduction. Characterization of charge environments at the nanoscale is very important for both fundamental research and practical applications, given its essential role in enhancing the sensitivity of biosensing [1] and chemical sensor applications [2]. Many advanced applications of diamond materials are now being limited by unknown surface defects, including in the fields of high power/frequency electronics, quantum computing [3,4], and quantum sensing [5]. Because of electric field screening and charge-state quenching of NV centers, elementary charge external to diamond is hard to be detected with nanoscale resolution [5,6]. It has been demonstrated that the NV center is the only system capable of imaging elementary charges at room temperatures with nanoscale precision [7,8]. In previous studies, the single charge to be detected either originated from the nearby second NV center [9] or from the substituted nitrogen atom. In this paper, we utilize the single NV center to showcase real-time tracking of single charge jump dynamics within diamond.

Apart from its applications in electrometry, the NV center finds extensive utility in various other fields including high-sensitivity nanomagnetometry [10–12] and thermometry [13–15]. In the majority of studies, the effective field is typically regarded as an undesirable attribute and is sought to be mitigated or minimized [16]. However, our investigation provide a new possibility: the directional symmetry exhibited by a single NV center with high effective field [17] may prove to be useful property. Even more intriguingly, there exist two tunable states that hold promise as a novel manipulation method for NV centers. Furthermore, when it comes to defining and understanding the mechanisms behind the effective field, most studies tend to attribute it solely to either strain or an electric field. Our experiments reveal that the strong effective field observed in individual NV centers is inconsistent with a pure electric field. It is imperative to consider the contribution of strain fields surrounding the charge traps to the high effective field [18].

Hamiltonian under high effective field. The NV center is a point defect in diamond consisting of a substitutional nitrogen atom situated adjacent to a carbon vacancy [19]. The NV coordinate system is given in Fig. 1(a), with the z axis along the NV axis and x axis perpendicular to the NV axis and in one of the symmetry plane. The Hamiltonian describing the ground state spin of the NV center in the presence of magnetic ($\mathbf{B}$) and effective field ($\mathbf{\Pi}$) is [20–22]

$$H = (D_{gs} + \Pi_\parallel)S_z^2 + \gamma_e \mathbf{B}\cdot\mathbf{S} + \mathbf{S}\cdot\mathbf{A_N}\cdot\mathbf{I_N} + \Pi_y(S_xS_y + S_yS_x) + \Pi_x\left(S_y^2 - S_x^2\right), \quad (1)$$

where $D = 2.87$ GHz is the zero-field splitting at room temperature, $\Pi_\parallel = d_\parallel E_z + \mathcal{M}_z$, $\Pi_{x,y} = d_\perp E_{x,y} + \mathcal{M}_{x,y}$, and $d_\parallel = 0.35(2)$ Hz/(V/cm) and $d_\perp = 17(3)$ Hz/(V/cm) are the electric field susceptibility parameters in the axial and transverse NV directions. The coupling parameter $\mathcal{M}_{x,y,z}$ is associated with the stress tensor [23]. $\gamma_e = 28$ MHz/mT is the NV spin's gyromagnetic ratio, and $\mathbf{S}$ are the NV spin-operators ($S = 1$). $\mathbf{A_N}$ is tensor relevant to the hyperfine interaction with the host ^{14}N($A_N \approx 2$ MHz) [24]. In Fig. 1(b), the ground-state spin energy level diagram of the NV center is presented under the conditions of $E_x \neq 0$ V/cm or $B_z \neq 0$ mT. The eigen-energies of the system are [25]

$$f_{m_S,\mu_N} = D_{gs} + \Pi_\parallel + m_S\sqrt{(\gamma_e B_z + \mu_N A_N)^2 + (\Pi_\perp)^2} \quad (2)$$

where $\Pi_\perp = \sqrt{\Pi_x^2 + \Pi_y^2}$.

Ramsey interferometry of the $|0\rangle \leftrightarrow |\pm\rangle$ transition is used to determine the on-resonsance MW frequency to a high degree of precision and accuracy [26]. The experiment is

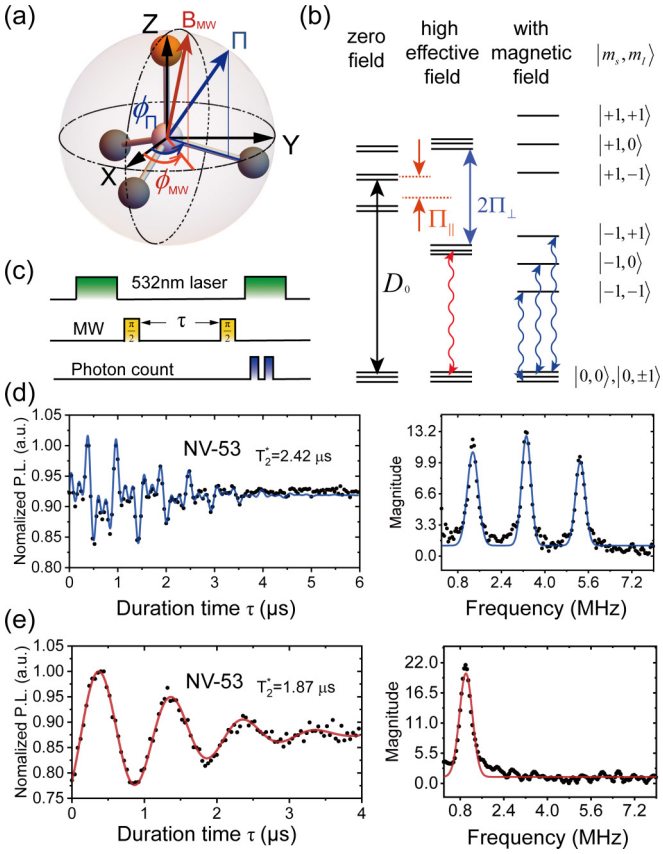

FIG. 1. (a) Coordinate system of the NV center with the relevant fields interacting with the NV spin: The MW magnetic field (in red) for spin manipulation, the effective field comprising strain and electric field (in blue) intrinsic to the diamond sample. (b) Level diagram of the NV ground state based on Hamiltonian (1) under different conditions. (c) Pulse sequences for Ramsey measurement. (d) Ramsey data showing a decay and multiple frequency components. Right panel is the fast fourier transformation (FFT) of the Ramsey oscillations. 2.2 MHz frequency splitting corresponds to hyperfine splitting caused by ^{14}N nuclear spin. (e) Ramsey data showing a decay and single frequency components. Right panel is the FFT of the Ramsey oscillations. (d) and (e) pertain to the same NV center, with the distinction that (d) is measured in the presence of a magnetic field.

performed by applying the sequence $(\frac{\pi}{2})_x - \tau - (\frac{\pi}{2})_x$, where τ is a variable free evolution time [Fig. 1(c)]. Ramsey fringes are characteristic of an NV center and its environment, yielding the free induction decay time, the hyperfine coupling with the N nuclear spin and the qubit energy splitting. In the regime where $B_z \gg \Pi_\perp$, the presence of three frequency components [Fig. 1(d)] in Ramsey signals arises from the energy level splitting induced by the hyperfine interaction with the ^{14}N nuclear spin. According to the Hamiltonian (1), when $\Pi_\perp \gg A_N$ and $B_z \approx 0$ mT, we can neglect the hyperfine interaction, which is suppressed by the high effective field [23]. The data are well reproduced by the fitting function [Fig. 1(e)]:

$$I = a \exp\left[\left(\frac{t}{T_2^*}\right)^2\right] \cos(2\pi\delta t + \phi) + b. \tag{3}$$

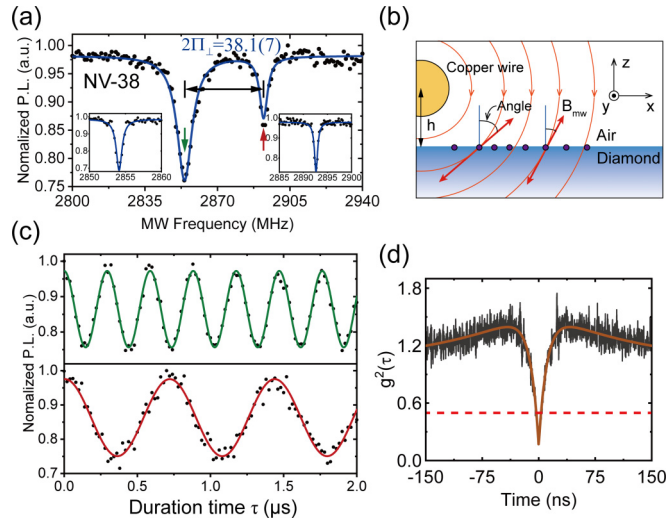

FIG. 2. (a) Continuous wave optically detected magnetic resonance (CW-ODMR) spectrum of the NV center with high effect field at zero magnetic field. (Left and right inset) Pulsed ESR spectroscopy of ^{14}NV resonances for the NV-38 (the NV centers are labeled according to their transverse splitting value $2\Pi_\perp$). The FWHM is far less than 2.2 MHz, indicating that the hyperfine energy level splitting caused by nitrogen spin is quite negligible. (b) Schematic representation of the distribution of the microwave magnetic field. The purple points are different measuring points of the same color center relative to the copper wire. The copper wire generates a linearly polarized microwave field oriented perpendicular to the copper wire and tangent to it. (c) Driving Rabi oscillations on each of the two on-resonance transitions. The frequency of Rabi oscillations is related to the angle of the microwave field (ϕ_{MW}) and the effective field (ϕ_Π). (d) Fluorescence autocorrelation function. $g^2(\tau) < 0.5$ definitively confirms it is a single NV center.

The oscillation of the Ramsey measurement is induced by a microwave with a detuning δ MHz from resonance. It is noteworthy that the dephasing time in the presence of magnetic field ($T_2^* = 2.42\ \mu$s) is longer than that in the absence of magnetic field ($T_2^* = 1.87\ \mu$s), which stems from the competition between surface electric field noise and magnetic field noise [27,28].

To quantify the influence of the effective field $\mathbf{\Pi}$ on the NV level structure, it is convenient to partition the field vectors into components parallel and perpendicular to the NV axis, i.e., to write $\mathbf{\Pi} = \{\Pi_\perp \cos\phi_\Pi, \Pi_\perp \sin\phi_\Pi, \Pi_\parallel\}$ [Fig. 1(a)]. We treat $\mathbf{B}_{MW}$ the same, with $B_\perp$, $B_\parallel$ and ϕ_{MW} defined similarly [Fig. 1(a)]. The direction of the electric field component within the plane perpendicular to the NV axis dictates the manner in which the $|m_s = \pm1\rangle$ states blend into bright and dark states as described below:

$$|\pm\rangle = \frac{1}{\sqrt{2}}(|m_s = +1\rangle \mp e^{-i\phi_\Pi}|m_s = -1\rangle). \tag{4}$$

Extract direction of effective field. Applying a linearly polarized microwave field will then drive transitions between the $|m_s = 0\rangle$ state and the $|\pm\rangle$ states. However, the relative strength of the two transitions depends on both ϕ_Π and the polarization of the microwave field, ϕ_{MW} [Fig. 2(a)]. Through a transformation to rotating frame and the application of

rotating wave approximation, the Rabi frequencies governing the resonant spin transitions between $|m_s = 0\rangle$ and $|\pm\rangle$, induced by the magnetic dipole interaction, can be expressed as follows [29]:

$$\Omega_{0,\pm} = \frac{2\pi}{h} |\langle \pm| - \mathbf{B}_{\mathrm{MW}} \cdot \boldsymbol{\mu} |0\rangle| = \frac{2\pi}{h} |\mathbf{B}_{\mathrm{MW}} \cdot \boldsymbol{\mu}_{0,\pm}|, \quad (5)$$

where the magnetic dipole moment operator is $\boldsymbol{\mu} = -h\gamma_e \mathbf{S} = -2\mu_B \mathbf{S}$ with μ_B being the Bohr magneton. The diamond sample used in our experiment was synthesized by the MPCVD method. Then the NV centers were generated near the surface through N ion implantation [30]. We developed a program to automatically perform fluorescence scans on our diamond sample and identified numerous single NV centers according to the fluorescence intensity, followed by automatic CW-ODMR scans of these centers. We carefully select those with strong effective fields as the subjects of our investigation, wherein the splitting of their spin levels can be directly observed through CW-ODMR [Fig. 2(a)]. As shown in Fig. 2(d), we measured the second-order correlation function $g^2(\tau)$ of the NV centers, excluding the influence of multiple color centers. To eliminate the influence of nuclear spins, we introduce a magnetic field to selected center or alter the orientation of the microwave field to observe whether the resonance peaks continue to split [23,31] or experience changes in imbalance [8,32]. In our experiment, the effective fields are sufficiently substantial, prompting us to extract the effective field orientation, by considering the ratio of Rabi frequencies (denoted as $\mathcal{R}$) at on-resonance conditions. From Eq. (5), we can deduce the relationship between $\mathcal{R}$ and the parameters $\{\phi_\Pi, \phi_{\mathrm{MW}}\}$ defining the field direction as follows [23]:

$$\mathcal{R} \triangleq \frac{\Omega_{0,+}}{\Omega_{0,-}} = \left| \tan\left(\frac{\phi_\Pi}{2} + \phi_{\mathrm{MW}}\right) \right|. \quad (6)$$

Through Eq. (6), for precise determination of the effective field's orientation, namely ϕ_Π, it is necessary to measure $\mathcal{R}$ under various microwave polarization directions relative to the NV coordinate system. To quantitatively vary the microwave polarization direction, we employ a copper wire with 20 μm diameter as our microwave antenna. The copper wire's length significantly exceeds the distance between the copper wire and the diamond surface [h ∼ 30 μm as shown in Fig. 2(b)], allowing it to be regarded as effectively infinite in length. To ensure the generation of highly polarized microwave vectors, our MW electronic circuits are designed to match the impedance of the antenna to reduce the total power reflection. As the relative permeability of diamond crystal is ∼1.0000, it can be approximated that the presence of diamond does not affect the spatial distribution and polarization direction of microwave field.

The magnitude of the microwave vector exhibits an inverse relationship with the distance to the wire, while its direction can be determined through the application of Ampere's theorem. To determine the effective field's orientation, we conduct measurements of the Rabi frequencies at various positions relative to the copper wire [Fig. 2(b)]. It's worth noting that the ratio of Rabi frequencies is independent of microwave power and solely depends on the directional parameters [23]. Therefore, we can optimize the microwave power to ensure that Rabi oscillations at different resonance frequencies exhibit noticeable periodic differences within the μs time frame at each measurement point [Fig. 2(c)]. The ratio of Rabi frequencies (6) at different points are obtained $(\mathcal{R}^i, i = 1, 2, \ldots, n)$. We define $(\hat{X}, \hat{Y}, \hat{Z})$ as our laboratory frame as shown in Fig. 2(b). The normalized directional vector of the NV axis with respect to the laboratory coordinate system is $\overrightarrow{\mathrm{NV}} = \{\sin(\theta)\cos(\phi), \sin(\theta)\sin(\phi), \cos(\theta)\}$, involving two unspecified parameters [23]. Our experimental dataset is overcomplete, allowing us to simultaneously determine the directions of the effective field and the NV axis using the least squares method. We employ the mean square error (MSE) function as the loss function, defined as follows (see the Supplemental Material [23] for more details):

$$\mathbf{F}_{\mathrm{MSE}} = \frac{1}{n} \sum_{i=1}^{n} \left[\left| \tan\left(\frac{\phi_\Pi}{2} + \phi^i_{\mathrm{MW}}\right) \right| - \mathcal{R}^i \right]^2. \quad (7)$$

Minimizing the MSE function using the simulated annealing method yields the optimal vector value.

Electric field vs strain field. The NV center spin is far more susceptible to transverse electric fields since $d_\perp \approx 50 d_\parallel$ [19], while all spin-stress coupling strength parameters $(\mathcal{M}_{x,y,z})$ are of comparable magnitude. Consequently, when the electric field dominates, the average impact of a randomly oriented electric field results in a significant splitting with negligible common-mode shift (i.e., $\Pi_\perp \gg \Pi_\parallel$, on average) [8]. Conversely, in the presence of a dominant strain field, the splitting is accompanied with a common-mode shift in the same order of magnitude (i.e., $\Pi_\perp \approx \Pi_\parallel$, on average) [29]. However, regarding the strain induced by a charge trap, as the NV center closely approaches, it encounters not only the influence of the electric field from the charge but also the impact of the localized strain originating from the trap. Moreover, when the charge is in close proximity to the NV center, it can only occupy some specific positions due to the constraints imposed by the diamond crystal structure. Hence, the direction of the high effective field caused by the charge trap is not arbitrary, but constrained by the crystal structure. The above analysis suggests a strong effective field, implying the charges located close to the NV centers. Considering the magnitude of the splitting (around 10 MHz) induced by the electric field from a charge (within 2 nm), any component of the strain or electric field in the strong effective field is not negligible. As illustrated in Figs. 3(a) and 3(e), almost all of the NV centers we observed have two states, and the average splitting and shifting have the same order of magnitude ($\overline{\Pi}_\perp \approx 21$ MHz, $\overline{\Pi}_\parallel \approx 13$ MHz). The comparable magnitudes between shifting and splitting suggests the presence of strain components in the effective field. We also observed that for individual color center NV-42, the ODMR spectrum shifting reached $\Pi_\parallel = 56.56$ MHz and the difference of the ODMR spectrum shifting of the two states amounted to $\Delta\Pi_\parallel = 37.14$ MHz [Fig. 3(e)]. The obvious change of effective field swapping between two values indicates the NV center is close to the charge trap, leading the electric field component in the effective field nonnegligible. By sweeping the polarization direction of MW driving field, we extracted $\Pi_\perp$ vectors for specific charge states, as illustrated in Fig. 3(c). Notably, distinct ODMR spectra are observed to correlate with different effective field directions. The two states most likely correspond to different

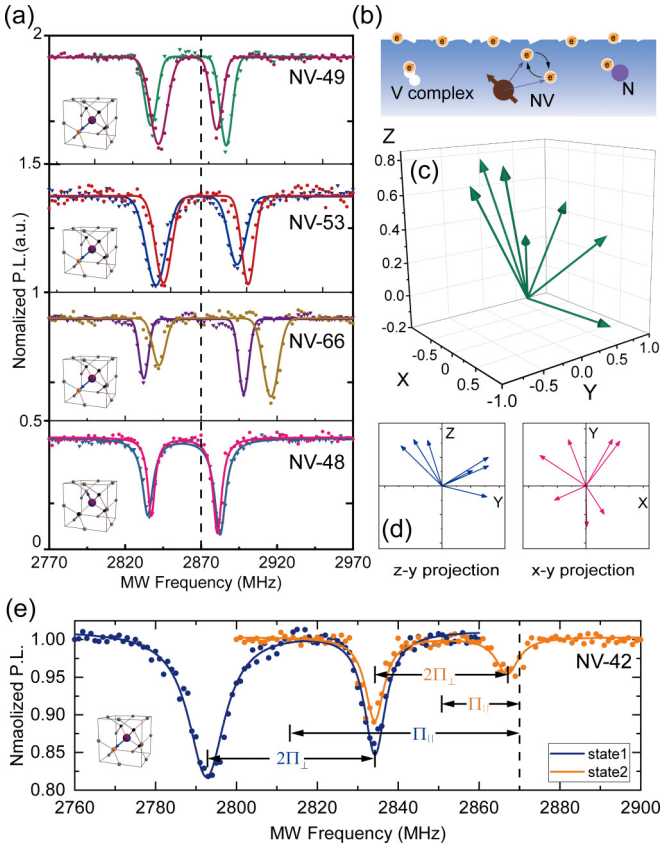

FIG. 3. (a) CW-ODMR for various NV centers in our experiment. Each center is associated with two distinct sets of curves. (b) Schematic diagram illustrating potential charged traps near the diamond surface and the impact of charge jumps on the effective field around the NV center. (c) The directional vectors for the transverse effective fields of several NV centers are collectively depicted in a single figure. The direction of the coordinate axes corresponds to those in Fig. 1(a). (d) Side and top views of (c). Due to the existence of four possible orientations for the NV center and the random relative positions of the NV center and charge trap, complete alignment was not observed. (e) CW-ODMR of the NV center in our experiment with ultralarge splitting [$2\Pi_\perp = 41.6(5)$ MHz, 33(1) MHz] and shifting. The dashed line indicates 2870 GHz.

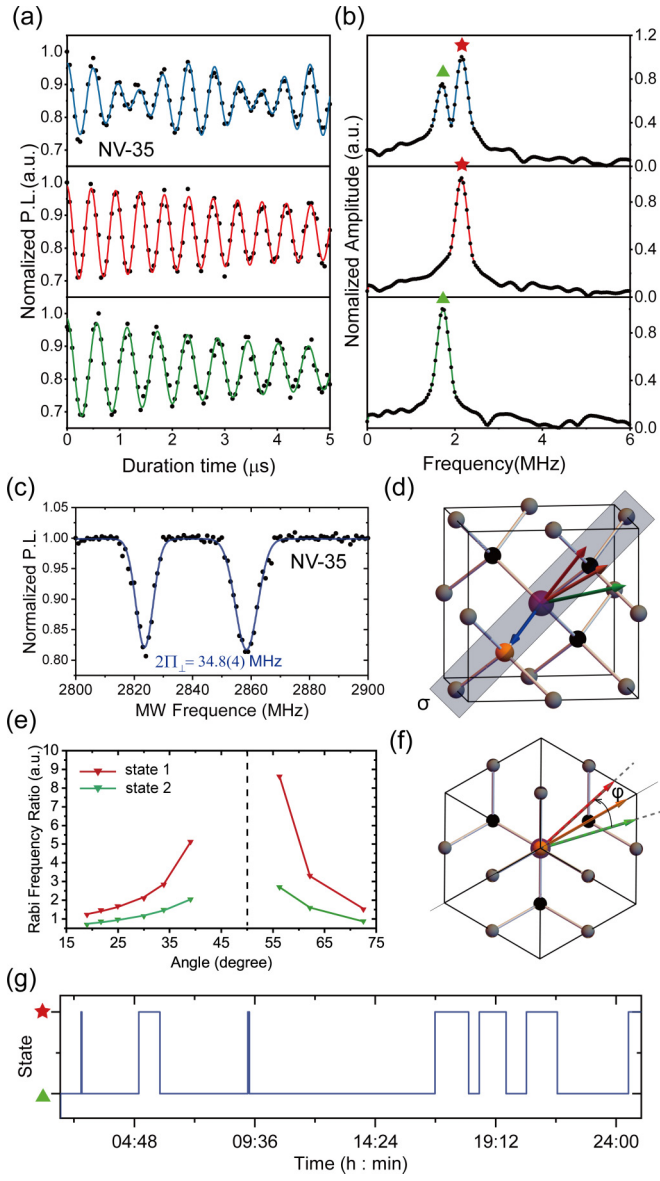

FIG. 4. (a) Rabi oscillations and (b) their corresponding Fourier transformation. The data (blue) with beat frequency results from the superposition of the following two data (red and green) points. (c) ODMR spectrum of the NV center with two states. The two charge positions correspond to the unique resonance spectrum. (d) Orientation of the NV center in the diamond unit cell and the vertical effective field corresponding to the different charge position. (e) The ratio of Rabi frequency for different microwave polarization. The horizontal axis represents the angle between the microwave vector and the z axis. When the angle approaches the dashed line in the figure, it indicates that the microwave vector and the transverse component of the effective field are nearly perpendicular. (f) The perspective along the NV direction in (b). Thus, demonstrating that the splitting of Rabi frequency originates from different charge configuration near the NV center. (g) The tracking measurement of Rabi frequency. The center changes randomly between the two charge states over time.

positions of charge relative to the NV center [Fig. 3(b)]. The characteristic time of NV centers under investigation switching between the two states ranges from tens of minutes to several hours, which corresponds to the random jumping of charge between two states near room temperature. Through prolonged observation and operation, the properties of these NV centers remain unchanged, indicating that these charge traps are stable structures.

Charge tracking. We also identified a unique center that cannot differentiate between different states through CW-ODMR [Fig. 3(a)] or Ramsey measurement [7,8], as the energy level structures of the two states are identical. However, Rabi oscillation has obvious beat frequency phenomenon, and the distinct frequency components can be separated by monitoring the data integration process [Fig. 4(a)]. As illustrated in Fig. 4(c), the two charge states share a common CW-ODMR. For a NV center in a certain direction, there are three planes of reflection [33]. When the two states of charges are mirror symmetrical with respect to the planes of reflection noted as σ, the parallel and perpendicular

components of the effective field relative to the NV axis remain unchanged [Fig. 4(d)]. To validate our interpretation, the direction of $\Pi_\perp$ is determined by measuring the ratio of Rabi frequencies (6) under various microwave directions and optimizing the loss function (7), as illustrated in Figs. 4(d) and 4(e). The effective field corresponding to the two charge states has an angle of $\varphi = 25.6^\circ$ relative to the NV center. The dashed line denoting the electric field intersects a quarter point along one side of the regular hexagon and exhibits symmetry relative to the σ plane [Fig. 4(f)]. This result validates our claim: the direction of the high effective field is not arbitrary but rather constrained by the symmetry of the crystal. These conclusions can also serve as crucial references for analyzing the microscopic structure of charge traps.

The ratios of the integrated intensities of the two FFT peaks are directly related to the probabilities that charge in either states during a measurement [Fig. 4(b)]. The consistent contrast of Rabi oscillation (≈30%) also shows that the frequency offset is not attributable to detuning [34]. Instead it arises from the change of effective field relative to the direction of the microwave vector's orientation [35]. By tracking the temporal evolution of the Rabi frequency, we can compute that the average rate of charge jumps between the two states (represented by a triangle and a pentagon, respectively) is approximately 0.55 per hour [Fig. 4(g)]. This phenomenon can be modeled using stochastic process theory, giving rise to a random telegraph signal (RTN) at the NV color center. Consequently, the charge jumps observed in our experiments are highly likely to be one of the sources contributing to RTN in semiconductors.

Conclusion and outlook. Combined with the evidence that a single NV color center has two sets of ODMR and two sets of Rabi oscillations that can be separated in time, we have successfully used an NV color center as an electrometer to detect the random jumping of charge between two states near room temperature. Therefore, using NV electrometry to track the behavior of a single charge under ambient conditions and the jumping rate of some charge is confirmed. Furthermore, we leverage the charge environment of the NV center to achieve significant angular adjustments of the effective field, thereby enhancing the capabilities for vector field detection utilizing NV centers. Specifically, the single crystal particle 3D rotation tracking technique based on nitrogen vacancy center sensing [36], which has been used to study the dependence of cell activity, will benefit from the research in this paper. In addition, our measurements offer direct insights into potential sources of low-frequency electrical noise [37,38] in the vicinity of the diamond surface. NV centers with strong effective fields can also function as probes for surface electrical noise spectrum measurements, owing to their effective suppression of magnetic field noise [39,40].

Sample details. A $3 \times 3 \times 1$ mm laboratory-made diamond sample was produced by growing a homemade CVD diamond layer on a diamond substrate in the [100] direction using a Seki AX5250S MPCVD apparatus. Prior to growth, the reaction chamber was evacuated to 3.6×10^{-5} Pa using a molecular pump, and a 15 minute plasma etching process with H_2/O_2 was performed to remove surface damage caused by polishing. The reaction gas mixture consisted of CH_4, H_2, and O_2, with CH_4 and H_2 first purified through a gas purification unit to remove residual N_2, achieving a purity level of 9N, while the purity of O_2 was 5N. During CVD growth, the $CH_4/O_2/H_2$ ratio, microwave power, pressure, and temperature were set to 50/5/500 sccm, 4000–4200 W, 150 torr, and 1000–1040 °C, respectively. After 100 hours of growth, a high-purity CVD diamond layer of approximately 1.3 mm thickness was obtained. The diamond substrate and CVD layer were separated using a laser, and the CVD layer was then cut into the desired size, with areas not covered by polycrystalline diamond being removed. Finally, the CVD layer was mechanically polished on both sides. After polishing, it was implanted with N_2^+ ions with an energy of 60 keV at an average depth of 40 nm. Under annealing conditions of 1050 °C, N ions and vacancies in diamond recombine to form NV centers.

Acknowledgments. This work was supported by the National Natural Science Foundation of China (Grants No. 11374280 and No. 50772110). This work was partially carried out at the USTC Center for Micro and Nanoscale Research and Fabrication.

[1] Y. K. Wu and T. Weil, Recent developments of nanodiamond quantum sensors for biological applications, Adv. Sci. **9**, 2200059 (2022).

[2] F. Patolsky, G. Zheng, and C. M. Lieber, Fabrication of silicon nanowire devices for ultrasensitive, label-free, real-time detection of biological and chemical species, Nat. Protoc. **1**, 1711 (2006).

[3] Z. Xu, Z.-q. Yin, Q. Han, and T. Li, Quantum information processing with closely-spaced diamond color centers in strain and magnetic fields [invited], Opt. Mater. Express **9**, 4654 (2019).

[4] S. Pezzagna and J. Meijer, Quantum computer based on color centers in diamond, Appl. Phys. Rev. **8**, 011308 (2021).

[5] M. S. J. Barson, L. M. Oberg, L. P. McGuinness, A. Denisenko, N. B. Manson, J. Wrachtrup, and M. W. Doherty, Nanoscale vector electric field imaging using a single electron spin, Nano Lett. **21**, 2962 (2021).

[6] L. M. Oberg, M. O. de Vries, L. Hanlon, K. Strazdins, M. S. J. Barson, M. W. Doherty, and J. Wrachtrup, Solution to electric field screening in diamond quantum electrometers, Phys. Rev. Appl. **14**, 014085 (2020).

[7] F. Dolde, M. W. Doherty, J. Michl, I. Jakobi, B. Naydenov, S. Pezzagna, J. Meijer, P. Neumann, F. Jelezko, N. B. Manson, and J. Wrachtrup, Nanoscale detection of a single fundamental charge in ambient conditions using the nv- center in diamond, Phys. Rev. Lett. **112**, 097603 (2014).

[8] T. Mittiga, S. Hsieh, C. Zu, B. Kobrin, F. Machado, P. Bhattacharyya, N. Z. Rui, A. Jarmola, S. Choi, D. Budker, and N. Y. Yao, Imaging the local charge environment of nitrogen-vacancy centers in diamond, Phys. Rev. Lett. **121**, 246402 (2018).

[9] A. Lozovoi, H. Jayakumar, D. Daw, G. Vizkelethy, E. Bielejec, M. W. Doherty, J. Flick, and C. A. Meriles, Optical activation

and detection of charge transport between individual colour centres in diamond, Nat. Electron. **4**, 717 (2021).
[10] H. Zheng, Z. Sun, G. Chatzidrosos, C. Zhang, K. Nakamura, H. Sumiya, T. Ohshima, J. Isoya, J. Wrachtrup, A. Wickenbrock, and D. Budker, Microwave-free vector magnetometry with nitrogen-vacancy centers along a single axis in diamond, Phys. Rev. Appl. **13**, 044023 (2020).
[11] J. F. Barry, J. M. Schloss, E. Bauch, M. J. Turner, C. A. Hart, L. M. Pham, and R. L. Walsworth, Sensitivity optimization for nv-diamond magnetometry, Rev. Mod. Phys. **92**, 015004 (2020).
[12] L. Rondin, J. P. Tetienne, T. Hingant, J. F. Roch, P. Maletinsky, and V. Jacques, Magnetometry with nitrogen-vacancy defects in diamond, Rep. Prog. Phys. **77**, 056503 (2014).
[13] M. Fujiwara and Y. Shikano, Diamond quantum thermometry: from foundations to applications, Nanotechnology **32**, 482002 (2021).
[14] G. Kucsko, P. C. Maurer, N. Y. Yao, M. Kubo, H. J. Noh, P. K. Lo, H. Park, and M. D. Lukin, Nanometre-scale thermometry in a living cell, Nature (London) **500**, 54 (2013).
[15] T. Plakhotnik, M. W. Doherty, J. H. Cole, R. Chapman, and N. B. Manson, All-optical thermometry and thermal properties of the optically detected spin resonances of the nv- center in nanodiamond, Nano Lett. **14**, 4989 (2014).
[16] J. S. Hodges, N. Y. Yao, D. Maclaurin, C. Rastogi, M. D. Lukin, and D. Englund, Timekeeping with electron spin states in diamond, Phys. Rev. A **87**, 032118 (2013).
[17] Y. Zhou, J. F. Wang, X. M. Zhang, K. Li, J. M. Cai, and W. B. Gao, Self-protected thermometry with infrared photons and defect spins in silicon carbide, Phys. Rev. Appl. **8**, 044015 (2017).
[18] W. Körner, D. F. Urban, and C. Elsasser, Influence of extended defects on the formation energy, hyperfine structure, and zero-field splitting of nv centers in diamond, Phys. Rev. B **103**, 085305 (2021).
[19] M. W. Doherty, N. B. Manson, P. Delaney, F. Jelezko, J. Wrachtrup, and L. C. L. Hollenberg, The nitrogen-vacancy colour centre in diamond, Phys. Rep. **528**, 1 (2013).
[20] P. Udvarhelyi, V. O. Shkolnikov, A. Gali, G. Burkard, and A. Palyi, Spin-strain interaction in nitrogen-vacancy centers in diamond, Phys. Rev. B **98**, 075201 (2018).
[21] D. A. Broadway, B. C. Johnson, M. S. J. Barson, S. E. Lillie, N. Dontschuk, D. J. McCloskey, A. Tsai, T. Teraji, D. A. Simpson, A. Stacey, J. C. McCallum, J. E. Bradby, M. W. Doherty, L. C. L. Hollenberg, and J. P. Tetienne, Microscopic imaging of the stress tensor in diamond using in situ quantum sensors, Nano Lett. **19**, 4543 (2019).
[22] M. S. J. Barson, P. Peddibhotla, P. Ovartchaiyapong, K. Ganesan, R. L. Taylor, M. Gebert, Z. Mielens, B. Koslowski, D. A. Simpson, L. P. McGuinness, J. McCallum, S. Prawer, S. Onoda, T. Ohshima, A. C. Bleszynski Jayich, F. Jelezko, N. B. Manson, and M. W. Doherty, Nanomechanical sensing using spins in diamond, Nano Lett. **17**, 1496 (2017).
[23] See Supplemental Material at http://link.aps.org/supplemental/10.1103/PhysRevB.109.224104 for additional data, numerics, and theory details.
[24] J. Wrachtrup and F. Jelezko, Processing quantum information in diamond, J. Phys.: Condens. Matter **18**, S807 (2006).
[25] N. Wang, C. F. Liu, J. W. Fan, X. Feng, W. H. Leong, A. Finkler, A. Denisenko, J. Wrachtrup, Q. Li, and R. B. Liu, Zero-field magnetometry using hyperfine-biased nitrogen-vacancy centers near diamond surfaces, Phys. Rev. Res. **4**, 013098 (2022).
[26] K. C. Miao, J. P. Blanton, C. P. Anderson, A. Bourassa, A. L. Crook, G. Wolfowicz, H. Abe, T. Ohshima, and D. D. Awschalom, Universal coherence protection in a solid-state spin qubit, Science **369**, 1493 (2020).
[27] M. Kim, H. J. Mamin, M. H. Sherwood, K. Ohno, D. D. Awschalom, and D. Rugar, Decoherence of near-surface nitrogen-vacancy centers due to electric field noise, Phys. Rev. Lett. **115**, 087602 (2015).
[28] P. Jamonneau, M. Lesik, J. P. Tetienne, I. Alvizu, L. Mayer, A. Dreau, S. Kosen, J. F. Roch, S. Pezzagna, J. Meijer, T. Teraji, Y. Kubo, P. Bertet, J. R. Maze, and V. Jacques, Competition between electric field and magnetic field noise in the decoherence of a single spin in diamond, Phys. Rev. B **93**, 024305 (2016).
[29] J. Kölbl, M. Kasperczyk, B. Burgler, A. Barfuss, and P. Maletinsky, Determination of intrinsic effective fields and microwave polarizations by high-resolution spectroscopy of single nitrogen-vacancy center spins, New J. Phys. **21**, 113039 (2019).
[30] F. P. Feng, J. F. Wang, W. L. Zhang, J. Zhang, L. R. Lou, W. Zhu, and G. Z. Wang, Efficient generation of nanoscale arrays of nitrogen-vacancy centers with long coherence time in diamond, Appl. Phys. A **122**, 944 (2016).
[31] C. Bengs and M. H. Levitt, Spindynamica: Symbolic and numerical magnetic resonance in a mathematica environment, Magn. Reson. Chem. **56**, 374 (2018).
[32] S. Blanes, F. Casas, J. A. Oteo, and J. Ros, The magnus expansion and some of its applications, Phys. Rep. **470**, 151 (2009).
[33] J. R. Maze, A. Gali, E. Togan, Y. Chu, A. Trifonov, E. Kaxiras, and M. D. Lukin, Properties of nitrogen-vacancy centers in diamond: the group theoretic approach, New J. Phys. **13**, 025025 (2011).
[34] R. Hanson, V. V. Dobrovitski, A. E. Feiguin, O. Gywat, and D. D. Awschalom, Coherent dynamics of a single spin interacting with an adjustable spin bath, Science **320**, 352 (2008).
[35] P. Wang, Z. Yuan, P. Huang, X. Rong, M. Wang, X. Xu, C. Duan, C. Ju, F. Shi, and J. Du, High-resolution vector microwave magnetometry based on solid-state spins in diamond, Nat. Commun. **6**, 6631 (2015).
[36] X. Feng, W. H. Leong, K. W. Xia, C. F. Liu, G. Q. Liu, T. Rendler, J. Wrachtrup, R. B. Liu, and Q. Li, Association of nanodiamond rotation dynamics with cell activities by translation-rotation tracking, Nano Lett. **21**, 3393 (2021).
[37] C. Noel, M. Berlin-Udi, C. Matthiesen, J. Yu, Y. Zhou, V. Lordi, and H. Haffner, Electric-field noise from thermally activated fluctuators in a surface ion trap, Phys. Rev. A **99**, 063427 (2019).
[38] B. L. Foulon, K. G. Ray, C. E. Kim, Y. Liu, B. M. Rubenstein, and V. Lordi, 1/omega electric-field noise in surface ion traps from correlated adsorbate dynamics, Phys. Rev. A **105**, 013107 (2022).
[39] S. Kolkowitz, A. Safira, A. A. High, R. C. Devlin, S. Choi, Q. P. Unterreithmeier, D. Patterson, A. S. Zibrov, V. E. Manucharyan, H. Park, and M. D. Lukin, Probing johnson noise and ballistic transport in normal metals with a single-spin qubit, Science **347**, 1129 (2015).
[40] P. Chrostoski, H. R. Sadeghpour, and D. H. Santamore, Electric noise spectra of a near-surface nitrogen-vacancy center in diamond with a protective layer, Phys. Rev. Appl. **10**, 064056 (2018).